Research Square

Preprints are preliminary reports that have not undergone peer review.
They should not be considered conclusive, used to inform clinical practice,
or referenced by the media as validated information.

Impact of Sub-Picosecond Timing Errors on Complex Conductivity Extraction in Terahertz Time-Domain Spectroscopy of Ultrathin FAPbI3 Films

Minhee Cha
Incheon National University
Junho Ryeom
Chung-Ang University
Bong Joo Kang
Korea Research Institute of Chemical Technology
Hajung Park
Incheon National University
Hyunbin Jang
Incheon National University
Sung Ju Hong
Kangwon National University
Young-Mi Bahk
ymb@inu.ac.kr

Incheon National University

Research Article

Keywords: terahertz spectroscopy, nano film, complex conductivity, organic-inorganic halide perovskite

Posted Date: April 17th, 2026

DOI: https://doi.org/10.21203/rs.3.rs-9269179/v1

License: This work is licensed under a Creative Commons Attribution 4.0 International License. Read Full License

Additional Declarations: No competing interests reported.

Version of Record: A version of this preprint was published at Journal of Infrared, Millimeter, and Terahertz Waves on July 29th, 2026. See the published version at https://doi.org/10.1007/s10762-026-01162-z.

Abstract

Terahertz time-domain spectroscopy (THz-TDS) is widely used to determine the complex conductivity of thin films from transmission measurements. For ultrathin films with thicknesses much smaller than the THz wavelength, however, the retrieved complex conductivity becomes highly sensitive to small phase errors in the measured transmission spectrum. In this work, we investigate the impact of sub-picosecond temporal uncertainty on the extraction of complex conductivity spectra in THz-TDS. Transmission measurements were performed on 400-nm-thick $FAPbI_3$ (Formamidinium Lead Iodide) films coated on dielectric substrates, and the spectra were analyzed using a Lorentz oscillator model. Small temporal offsets between sample and reference waveforms introduce systematic phase errors that predominantly affect the imaginary component of the conductivity. Numerical analysis shows that temporal deviations on the order of tens of femtoseconds can lead to significant distortions in the retrieved conductivity spectra. The analysis further indicates that these phase errors primarily modify the high-frequency permittivity parameter in Lorentz oscillator fitting, while the resonance frequency, oscillator strength, and damping constant remain largely unaffected. A phase-correction procedure is demonstrated to mitigate these effects and improve the reliability of conductivity extraction for nanometer-scale films. These results highlight the importance of precise phase alignment in THz-TDS of ultrathin materials.

1 INTRODUCTION

Terahertz time-domain spectroscopy (THz-TDS) has emerged as a powerful technique for probing the low-energy electrodynamic response of materials [1–6]. By measuring both the amplitude and phase of the transmitted THz electric field, THz-TDS enables the direct determination of the complex refractive index and conductivity without requiring Kramers–Kronig transformations. Owing to these advantages, THz-TDS has been widely employed to investigate charge carrier dynamics, phonon resonances, and transport properties in semiconductors, superconductors, and quantum materials [7–12].

In recent years, THz spectroscopy of ultrathin films has attracted increasing attention, particularly for two-dimensional materials and solution-processed semiconductors such as hybrid perovskites (e.g., $MAPbI_3$, $FAPbI_3$) [13–18]. When film thickness is much smaller than the THz wavelength, the thin-film approximation can be applied, allowing the complex sheet conductivity to be extracted from transmission measurements [19, 20]. Under these conditions, however, the retrieved conductivity becomes highly sensitive to small phase uncertainties in the measured transmission function [21–23]. Even minor phase errors can lead to significant deviations, particularly in the imaginary component of the conductivity.

In practical THz-TDS experiments, phase errors can arise from several sources, including substrate thickness mismatch between reference and sample measurements, mechanical drift of the system, and temporal offsets caused by timing jitter. These timing errors are typically on the order of tens of femtoseconds and are often negligible for bulk materials [2, 21]. For nanometer-scale films, however, such small temporal deviations can introduce measurable phase distortions in the transmission spectrum, thereby degrading the accuracy of the extracted conductivity. Despite their practical importance, the quantitative impact of sub-picosecond timing errors on conductivity extraction in ultrathin-film THz spectroscopy has not been systematically investigated.

In this work, we investigate the impact of sub-picosecond timing errors on complex conductivity extraction in THz-TDS measurements of ultrathin films. Transmission measurements were performed on 400-nm-thick

$FAPbI_3$ films coated on dielectric substrates. We analyze how small temporal offsets between the sample and reference waveforms introduce systematic phase distortions and demonstrate that timing deviations on the order of tens of femtoseconds significantly affect the imaginary component of the conductivity spectrum. A phase-correction approach is implemented to mitigate these errors and improve the robustness of conductivity retrieval. Furthermore, the analysis shows that phase errors predominantly influence the high-frequency permittivity parameter in Lorentz oscillator fitting, while the resonance frequency, oscillator strength, and damping constant remain largely unaffected.

2 EXPERIMENTAL RESULTS AND DISCUSSIONS

2.1 Terahertz Time-Domain Spectroscopy (THz-TDS)

A transmission-mode THz-TDS system was employed to measure the optical constants of the ultrathin film, as illustrated in Fig. 1a. The system is driven by a Ti:sapphire femtosecond laser delivering 94 fs pulses at a repetition rate of 84 MHz, centered at 800 nm with a spectral bandwidth of 10 nm and an average power of 1 W. The laser output is split into pump and probe beams. The pump beam excites a photoconductive antenna fabricated on a low-temperature-grown GaAs substrate to generate THz pulses [24–27]. The transmitted THz electric field is detected by electro-optic sampling in a 1-mm-thick ZnTe crystal using the probe beam [28–31]. The time-domain waveform is acquired by scanning an optical delay line, and the corresponding frequency-domain spectra are obtained via fast Fourier transform (FFT). The transmission function is defined as the ratio of the sample signal to the reference signal, where the reference corresponds to the bare substrate (1-mm-thick z-cut quartz). The measured amplitude and phase enable extraction of the complex optical constants and conductivity of the ultrathin film.

2.2 Sample Preparation

The *α*-phase $FAPbI_3$ was selected as a representative ultrathin-film material exhibiting Lorentz-type resonant behavior in the THz spectral range. This material has an ABX_3 perovskite structure, where A = formamidinium (FA), B = Pb, and X = I, as illustrated in Fig. 1b. The *α*-phase adopts a cubic crystal structure and is stable above ~ 300 K [32–37].

Ultrathin $FAPbI_3$ films were fabricated using a solution-based spin-coating process. $FAPbI_3$ powder was synthesized from FAI and PbI_2 precursors, followed by vacuum filtration with ethyl acetate washing solvent and thermal annealing to enhance crystallinity [36]. The precursor solution was prepared by dissolving 800 mg of $FAPbI_3$, 30 mg of $MAPbBr_3$, and 30 mg of MACl in a mixed solvent of 0.8 mL N, N-dimethylformamide (DMF) and 0.1 mL dimethyl sulfoxide (DMSO). The solution was filtered through a 0.2 μm PTFE filter prior to deposition. The solution was spin-coated onto 1-mm-thick z-cut quartz substrates, followed by dynamic dispensing of 1 mL diethyl ether to induce rapid crystallization. The films were annealed at 100°C for 40 min and subsequently at 150°C for 5 min to form the cubic *α*-phase. Finally, high-quality microcrystals of *α*-phase $FAPbI_3$ can be obtained from washing solvent and annealing method.

Figure 1c shows the top-view and cross-sectional view of scanning electron microscopy (SEM) images of the film. A compact polycrystalline morphology with well-defined grains is observed. The film thickness is

approximately 400 nm, as estimated from the cross-sectional image. The annealing process improves crystallinity and promotes uniform film formation.

2.3 THz Spectroscopy of $FAPbI_3$

Figure 1d shows the measured time-domain THz electric fields for the reference quartz substrate (gray) and the $FAPbI_3$ film (orange). While the overall pulse shapes are similar, a slight temporal shift and waveform distortion are observed in the sample signal. The inset highlights a temporal offset of 0.02 ps at the main peak position, which corresponds to the sampling interval. In addition to the slight reduction in the main peak amplitude, weak oscillatory features are also observed in the trailing region of the pulse, indicating resonant interactions within the film.

The time-domain signals were transformed into the frequency domain using FFT to obtain the transmission amplitude and phase spectra, as shown in Figs. 1e and 1f, respectively. The amplitude spectrum exhibits pronounced resonant absorption features near 0.9 THz and 1.7 THz, accompanied by rapid phase variations at the same frequencies (Fig. 1g).

The THz response of α-phase $FAPbI_3$ is governed by low-energy lattice vibrations of the Pb–I framework [15, 38–43]. The resonance near 1 THz is attributed to a transverse optical (TO) phonon mode associated with Pb–I–Pb bending vibrations, while the resonance around 2 THz corresponds to a longitudinal optical (LO) phonon mode related to Pb–I stretching vibrations (Fig. 1h) [41–43]. The LO mode is particularly sensitive to the orientation and rotational dynamics of A-site cations under the THz electric field [39, 44].

These resonant response serves as the basis for extracting the complex conductivity and dielectric parameters using the Lorentz oscillator model in the following section.

2.4 Influence of Substrate Mismatch and Temporal Offset on THz Transmission

To identify the origin of phase uncertainty in the transmission spectra, we first examine the effect of substrate thickness mismatch between the reference and sample measurements. Figure 2a shows the time-domain THz electric field signals for the reference substrate and two samples (Sample 1 and Sample 2). Although the overall pulse shapes are similar, a small shift in the peak position is observed, as highlighted in the inset. Such temporal differences arise from variations in optical path length, for example due to slight differences in substrate thickness.

A closer inspection shows that the peak of Sample 2 is delayed by approximately 0.06 ps relative to the reference, whereas Sample 1 is nearly aligned. This delay indicates a thicker substrate for Sample 2. Using the refractive index of quartz ($n \sim 1.96$) and a nominal thickness of 1 mm, the observed delay corresponds to an estimated substrate thickness of ~ 1025 μm for Sample 2. Direct measurement using a vernier caliper yields a thickness difference of ~ 30 μm, in good agreement with the THz-based estimation.

The corresponding frequency-domain spectra obtained via FFT are shown in Figs. 2b and 2c. While the amplitude spectra is similar, the phase difference between Sample 1 and Sample 2 exhibits a linear frequency dependence over the 0.5–2.5 THz range (inset of Fig. 2c). This behavior indicates that a temporal shift in the time-domain waveform introduces a systematic phase offset in the frequency domain.

To further quantify the effect of sub-picosecond timing uncertainty, the measured waveform of Sample 1 was artificially shifted in time by applying controlled temporal offsets. Figure 2d shows the resulting waveforms for negative (−), nominal, and positive (+) time shifts. The applied offset was ± 0.02 ps, corresponding to the sampling interval of the THz-TDS system. Despite the small magnitude of the shift, clear differences emerge in the corresponding frequency-domain response.

The resulting transmission amplitude and phase spectra are shown in Figs. 2e and 2f, respectively. The amplitude spectra show negligible variation, whereas the phase spectra exhibit pronounced frequency-dependent deviation induced by the temporal offset. This behavior follows the linear relationship between time delay and phase shift, given by

$$\Delta\varphi(\omega) = \omega\Delta t$$

where Δt is the temporal offset between the reference and sample waveforms. As a result, even a small timing error leads to a phase deviation that increases linearly with frequency [45–47].

These results demonstrate that sub-picosecond timing deviations produce measurable phase distortions in THz transmission spectra. This sensitivity is particularly critical for ultrathin films, where the extraction of complex optical properties relies strongly on accurate phase information. Precise temporal alignment between reference and sample waveforms is therefore essential for reliable conductivity analysis, particularly when timing uncertainties approach the tens-of-femtoseconds regime [45, 46]. As shown in the following section, such phase errors significantly influence the extraction of complex conductivity and dielectric parameters.

2.5 Extraction of Optical Constants and Complex Conductivity

The complex optical properties of the ultrathin film were extracted from the measured THz transmission spectra [2, 48, 49]. In transmission-mode THz-TDS, the complex transmission function is defined as

$$t(\omega) = E_{\text{sample}}(\omega)/E_{\text{ref}}(\omega)$$

where $E_{\text{sample}}(\omega)$ and $E_{\text{ref}}(\omega)$ are the Fourier-transformed electric fields transmitted through the sample and reference substrate, respectively.

The optical constants were determined using a transfer-function formalism that accounts for multiple reflections within the film–substrate structure [48–50]. In this approach, the complex refractive index $n(\omega)$ is obtained from the measured transmission function with a theoretical multilayer model. Since delayed internal reflections in the time domain signal are removed through the temporal windowing, the substrate thickness is considered to be effectively infinite. The refractive index is expressed as $n(\omega) = n + i\kappa$, where n and κ denote the real refractive index and extinction coefficient, respectively.

The complex dielectric function is then calculated as

$$\varepsilon(\omega) = n^2(\omega)$$

and the complex conductivity $\sigma(\omega)$ is obtained from

$$\sigma(\omega) = -i\omega\varepsilon_0[\varepsilon(\omega) - 1]$$

where ε_0 is the vacuum permittivity.

Figure 3 summarizes the extracted refractive index, dielectric constant, and conductivity obtained before and after the timing-error correction. While the overall spectral features are preserved, systematic deviations are observed depending on the applied temporal offset.

The extracted spectra exhibit characteristic features of a Lorentz-type response. Resonance peaks appear in the imaginary parts of the refractive index and dielectric function, as well as in the real part of the conductivity, corresponding to phonon resonances in the THz frequency range. In contrast, the real part of the refractive index and dielectric function, together with the imaginary part of the conductivity, show dispersive behavior near the resonance frequencies.

Although the spectral shapes remain similar, noticeable baseline shifts are observed under different timing conditions. This indicates that temporal misalignments primarily affect the background permittivity, such as the static or high-frequency dielectric constant, rather than the resonance structure itself.

A pronounced deviation is observed for the − 0.02 ps timing offset, where the high-frequency response becomes strongly distorted and the extracted conductivity exhibits unphysical negative values above 2 THz. This result highlights that even femtosecond-scale timing errors can lead to qualitatively incorrect conductivity spectra. The corresponding dataset was therefore excluded from subsequent Lorentz oscillator fitting.

2.6 Lorentz Oscillator Model Fitting

To quantitatively analyze the extracted spectra, the complex dielectric response was modeled using a Lorentz oscillator formalism. The frequency-dependent dielectric function is given by

$$\epsilon\ (\omega\ ) = \epsilon_{\infty}\ + \sum\ _{j} \frac{\omega\ _{p,j}^{2}}{\omega\ _{0,j}^{2} - \omega\ ^{2} - i\gamma\ _{j}\omega}$$

where ϵ_{∞} is the high-frequency dielectric constant, $\omega_{0,j}$ is the resonance frequency, $\omega_{p,j}$ is the oscillator strength, and γ_{j} is the damping constant of the *j*-th oscillator. In this study, two oscillators were used to describe the phonon resonances observed in the THz range.

The fitting was performed simultaneously on the dielectric function and conductivity spectra to ensure internal consistency of the extracted parameters [15, 38, 41].

Figures 4a and 4b show the real part of the conductivity (dotted lines) together with the corresponding Lorentz model fits (solid lines) before and after timing correction (+ 0.02 ps), respectively. The model reproduces the main spectral features well, including the phonon resonance peaks. Two resonances located near 0.9 THz and 1.7 THz are clearly identified, and the corresponding oscillator strengths and damping constants are extracted (Table 1).

Notably, the fitting parameters associated with the resonances (ω_{0}, ω_{p}, γ) show only minor variations between the corrected and uncorrected datasets. This indicates that the intrinsic phonon properties are largely insensitive to sub-picosecond timing errors.

In contrast, significant differences are observed in the baseline of the dielectric response. Figure 4c shows the real part of the dielectric constant and the corresponding model fits. While the resonance features are well reproduced in both cases, the extracted background permittivity differs substantially. As summarized in Table 1, the uncorrected dataset yields unphysical values of ϵ_{DC} and ϵ_{∞} (approximately − 13), whereas the corrected data produce values around 33, which are consistent with literature reports [38, 39, 41]. These results demonstrate that timing-induced phase errors predominantly affect the background permittivity, while leaving the resonance parameters largely unchanged. This selective sensitivity explains why small temporal misalignments can lead to significant errors in extracted conductivity, despite minimal changes in the apparent spectral features.

Figure 5a presents the extracted DC and high-frequency dielectric constant as a function of the applied temporal offset, including the raw dataset and three timing-corrected cases. In all cases, significant variations are observed. As the timing correction increases in the positive direction, the dielectric constant exhibits an approximately linear trend, which can be evaluated in terms of its physical plausibility. These results highlight the critical importance of phase correction through precise temporal alignment.

The Lorentz oscillator fitting parameters were also analyzed under different timing corrections. The resonance frequencies, oscillator strengths and damping constants remain nearly unchanged across all cases, indicating that the intrinsic phonon energies are robust against timing errors. These results demonstrate that, while the resonance features of the conductivity spectra are reliably reproduced, the background dielectric response is highly sensitive to small timing uncertainties in the time-domain measurement. The timing error introduces a frequency-dependent phase shift proportional to $\omega\Delta t$, which manifests as a global phase tilt in the frequency domain. Since resonance-related parameters (ω_0, ω_p, γ) are primarily determined by local spectral features, they remain unaffected. In contrast, ϵ_{∞} governs the high-frequency asymptotic behavior and effectively defines the global baseline of the dielectric response. Consequently, ϵ_{∞} is particularly susceptible to timing-induced phase distortions, leading to significant deviations even for sub-picosecond timing errors, thereby imposing stringent requirements on temporal alignment in ultrathin-film THz-TDS measurements.

3. CONCLUSIONS

In this work, we investigated the influence of sub-picosecond timing errors on the extraction of optical properties from transmission-mode THz-TDS measurements of ultrathin $FAPbI_3$ films. Experimental and numerical analyses show that small temporal offsets between the reference and sample waveforms introduce a frequency-dependent phase shift proportional to $\omega\Delta t$, leading to systematic distortions in the retrieved optical constants.

The extracted refractive index, dielectric function, and complex conductivity spectra exhibit characteristic resonant features that are well described by a Lorentz oscillator model. Two phonon resonances near 0.9 THz and 1.7 THz were consistently identified. The corresponding resonance parameters, including resonance frequency, oscillator strength, and damping constant, remain largely unaffected by small timing offsets, indicating that intrinsic phonon properties are robust against sub-picosecond temporal errors.

In contrast, the background dielectric parameters, particularly the high-frequency dielectric constant ϵ_{∞}, are highly sensitive to timing errors. Even temporal deviations on the order of tens of femtoseconds can significantly

alter the baseline of the dielectric response, resulting in substantial variations in the extracted permittivity. These results highlight the critical importance of precise temporal alignment in THz spectroscopy of ultrathin films. The findings provide practical guidance for reliable conductivity and dielectric parameter extraction and underscore the necessity of accurate phase correction in THz-TDS analysis of nanometer-scale materials.

Declarations

Declarations Competing Interests:

The authors declare no conflicts of interest.

Author Contribution

The experimental concept was conceived by Y.-M.B. B.J.K. prepared samples and M.C. and H.P. performed THz time-domain spectroscopy. M.C., J.R., H.J., and Y.-M.B. analyzed the results and M.C., J.R. and Y.-M.B. prepared the manuscript based on discussions with S.J.H. and B.J.K. All the authors have given their approval to the final version of the manuscript.

ACKNOWLEDGEMENT

This work is supported by an Incheon National University Research under Grant No. 2023 – 0138.

Data Availability

The data that support the findings of this study are available from the corresponding author upon reasonable request.

References

1. M. Tonouchi, “Cutting-edge terahertz technology,” Nat. Photonics 1(2), 97–105 (2007).
2. J. Lloyd-Hughes, and T.-I. Jeon, “A Review of the Terahertz Conductivity of Bulk and Nano-Materials,” J. Infrared, Millim. Terahertz Waves 33(9), 871–925 (2012).
3. H. J. Joyce, C. J. Docherty, Q. Gao, H. H. Tan, C. Jagadish, J. Lloyd-Hughes, L. M. Herz, and M. B. Johnston, “Electronic properties of GaAs, InAs and InP nanowires studied by terahertz spectroscopy,” Nano. Tech. 24(21), 214006 (2013).
4. M. Koch, D. M. Mittleman, J. Ornik, and E. Castro-Camus, “Terahertz time-domain spectroscopy,” Nat. Rev. Methods Primers 3(1), 48 (2023).
5. D. Grischkowsky, S. Keiding, M. Van Exter, and C. Fattinger, “Far-infrared time-domain spectroscopy with terahertz beams of dielectrics and semiconductors,” J. Opt. Soc. Am. B. 7(10), 2006–2015 (1990).
6. M. Heyden, J. Sun, S. Funkner, G. Mathias, H. Forbert, M. Havenith, and D. Marx, “Dissecting the THz spectrum of liquid water from first principles via correlations in time and space,” Proc. Natl. Acad. Sci. U.S.A. 107(27), 12068–12073 (2010).

7. A. von Hoegen, R. Mankowsky, M. Fechner, M. Först, and A. Cavalleri, “Probing the interatomic potential of solids with strong-field nonlinear photonics,” Nature 555(7694), 79–82 (2018).
8. E. Cinquanta, D. Meggiolaro, S. G. Motti, M. Gandini, M. J. Alcocer, Q. A. Akkerman, C. Vozzi, L. Manna, F. D. Angelis, A. Petrozza, and S. Stagira, “Ultrafast THz probe of photoinduced polarons in lead-halide perovskites,” Phys. Rev. Lett. 122(16), 166601 (2019).
9. R. L. Milot, G. E. Eperon, H. J. Snaith, M. B. Johnston, and L. M. Herz, “Temperature-dependent charge-carrier dynamics in $CH_3NH_3PbI_3$ perovskite thin films,” Adv. Funct. Mater. 25(39), 6218–6227 (2015).
10. P. Kuzel, and J. Petzelt, “Time-resolved terahertz transmission spectroscopy of dielectrics,” Ferroelectrics 239(1), 79–86 (2000).
11. A. Pashkin, M. Porer, M. Beyer, K. W. Kim, A. Dubroka, C. Bernhard, X. Yao, Y. Dagan, R. Hackl, A. Erb, J. Demsar, R. Huber, and A. Leitenstorfer, “Femtosecond response of quasiparticles and phonons in superconducting YBa2Cu3O7-δ studied by wideband terahertz spectroscopy,” Phys. Rev. Lett. 105(6), 067001 (2010).
12. A. Liu, “Multidimensional terahertz probes of quantum materials,” npj Quantum Mater. 10(1), 18 (2025).
13. D. T. Cuzzupè, F. Ünlü, K. Lê, R. Bernhardt, M. Wilhelm, Grosch, M. Grosch, R. Weißing, T. Fischer, Paul H. M. Loosdrecht and S. Mathur, “Thermally-induced drift of A-site cations at solid–solid interface in physically paired lead halide perovskites,” Sci. Rep. 12(1), 10241 (2022).
14. H. El-Ghtami, A. Laref, and S. Laref, “Electronic and optical behaviors of methylammonium and formamidinium lead trihalide perovskite materials,” J. Mater. Sci.: Mater. Electron. 30(1), 711–720 (2019).
15. I. Maeng, S. Lee, E. Q. Han, Y. Zhang, S. J. Oh, M. Nakamura, J.-H. Yun, L. Wang, Y.-K. Kwon, and M.-C. Jung, “Unusual terahertz-wave absorptions in δ/α-mixed-phase $FAPbI_3$ single crystals: interfacial phonon vibration modes,” NPG Asia Mater. 13(1), 75 (2021).
16. G. E. Eperon, S. D. Stranks, C. Menelaou, M. B. Johnston, L. M. Herz, and H. J. Snaith, “Formamidinium lead trihalide: a broadly tunable perovskite for efficient planar heterojunction solar cells,” Energy Environ. Sci. 7(3), 982–988 (2014).
17. J. Ryeom, D. Y. Park, Y.-M. Bahk, G. Choi, and M. S. Jeong, “Layer-dependent characterization of two-dimensional lead-halide perovskite crystals,” J. Alloys Compd. 1030, 180811 (2025).
18. J. Xu, Y. Wu, S. Fan, X. Liu, Z. Yin, Y. Yang, R. Wang, Z. Qian, and Y. Sun, “Real-time detection of aging status of methylammonium lead iodide perovskite thin films by using terahertz time-domain spectroscopy,” Front. Optoelectron. 17(1), 24 (2024).
19. Y. Takahashi, S. Chakraverty, M. Kawasaki, H. Hwang, and Y. Tokura, “In-plane terahertz response of thin film Sr_2RuO_4,” Phys. Rev. B 89(16) 165116 (2014).
20. M. Walther, D. G. Cooke, C. Sherstan, M. Hajar, M. R. Freeman, and F. A. Hegmann, “Terahertz conductivity of thin gold films at the metal-insulator percolation transition,” Phys. Rev. B. Condens. Matter Mater. Phys. 76(12), 125408 (2007).
21. L. Duvillaret, F. Garet, and J.-L. Coutaz, “Highly precise determination of optical constants and sample thickness in terahertz time-domain spectroscopy”, Appl. Opt. 38(2), 409–415 (1999).
22. C.-Y. Jen, and C. Richter, “Sample Thickness Measurement with THz-TDS: Resolution and Implications,” J. Infrared, Millim. Terahertz Waves 35(10), 840–859 (2014).

23. W. Withayachumnankul, B. M. Fischer, and D. Abbott, “Material thickness optimization for transmission-mode terahertz time-domain spectroscopy,” Opt. express 16(10), 7382–7396 (2008).
24. P. R. Smith, D. H. Auston, and M. C. Nuss, “Subpicosecond photoconducting dipole antennas,” IEEE J. Quantum Electron. 24(2), 255–260 (2002).
25. M. Tani, S. Matsuura, K. Sakai, and S. I. Nakashima, “Emission characteristics of photoconductive antennas based on low-temperature-grown GaAs and semi-insulating GaAs,” Appl. Opt. 36(30), 7853–7859 (1997).
26. E. S. Harmon, M. R. Melloch, J. M. Woodall, D. D. Nolte, Otsuka, N. Otsuka, and C. L. Chang, “Carrier lifetime versus anneal in low temperature growth GaAs,” Appl. Phys. Lett. 63(16), 2248–2250 (1993).
27. H. Nemec, A. Pashkin, P. Kuzel, M. Khazan, S. Schnull, and I. Wilke, “Carrier dynamics in low-temperature grown GaAs studied by terahertz emission spectroscopy,” J. Appl. Phys. 90(3), 1303–1306 (2001).
28. Q. Wu, and X. C. Zhang, “Free-space electro-optic sampling of terahertz beams,” Appl. Phys. Lett. 67(24), 3523–3525 (1995).
29. A. Nahata, D. H. Auston, T. -F. Heinz, and C. Wu, “Coherent detection of freely propagating terahertz radiation by electro-optic sampling,” Appl. Phys. Lett. 68(2), 150–152 (1996).
30. Paul C. M. Planken, H.-K. Nienhuys, H. J. Bakker, and T. Wenckebach, “Measurement and calculation of the orientation dependence of terahertz pulse detection in ZnTe,” J. Opt. Soc. Am. B. 18(3), 313–317 (2001).
31. G. Gallot, and D. Grischkowsky, “Electro-optic detection of terahertz radiation”, J. Opt. Soc. Am. B. 16(8), 1204–1212 (1999).
32. B. Kim, J. Kim, and N.-G. Park, “First-principles identification of the charge-shifting mechanism and ferroelectricity in hybrid halide perovskites,” Sci. Rep. 10(1), 19635 (2020).
33. Y. An, J. Hidalgo, C. A. R. Perini, A.-F. Castro-Mendez, J. N. Vagott, K. Bairley, S. Wang, X. Li, and J.-P. Correa-Baena, “Structural Stability of Formamidinium- and Cesium-Based Halide Perovskites,” ACS Energy. Lett. 6(5), 1942–1969 (2021).
34. H.-S. Kim, and N.-G. Park, “Soft Lattice and Phase Stability of α-$FAPbI_3$,” Adv. Energy Mater. 15(2), 2400089 (2025).
35. M. T. Weller, O. J. Weber, J. M. Frost, and A. Walsh, “Cubic perovskite structure of black formamidinium lead iodide, α-[$HC(NH_2)_2$] PbI_3 at 298 K,” J. Phys. Chem. Lett. 6(16), 3209–3212 (2015).
36. H. S. Kim, H.-S. Yun, C.-E. Seo, S. B. Yoo, B. J. Kang, E. H. Jung, and N. J. Jeon, “Ethanol purification enables high-quality α-phase $FAPbI_3$ perovskite microcrystals for commercial photovoltaic applications,” Nanoscale Horiz. 9(7), 1120–1127 (2024).
37. J. Yin, G. Teobaldi, and L. M. Liu, “The role of thermal fluctuations, and vibrational entropy: A theoretical insight into the δ-to-α transition of $FAPbI_3$,” J. Phys. Chem. Lett. 13(13), 3089–3095 (2022).
38. M. Sendner, P. K. Nayak, D. A. Egger, S. Beck, C. Muller, B. Epding, W. Kowalsky, L. Kronik, H. J. Snaith, A. Pucci, and R. Lovrincic, “Optical phonons in methylammonium lead halide perovskites and implications for charge transport,” Mater. Horiz. 3(6), 613–620 (2016).
39. M. Nagai, T. Tomioka, M. Ashida, M. Hoyano, R. Akashi, Y. Yamada, T. Aharen, and Y. Kanemitsu, “Longitudinal optical phonons modified by organic molecular cation motions in organic-inorganic hybrid perovskites,” Phys. Rev. Lett. 121(14), 145506 (2018).
40. C. L. Davies, J. Borchert, C. Q. Xia, R. L. Milot, H. Kraus, M. B. Johnston, and L. M. Herz, “Impact of the organic cation on the optoelectronic properties of formamidinium lead triiodide,” J. Phys. Chem. Lett. 9(16),

4502–4511 (2018).

41. C. La-o-vorakiat, H. Xia, J. Kadro, T. Salim, D. Zhao, T. Ahmed, Y. M. Lam, J.-X. Zhu, R. A. Marcus, M.-E. Michel-Beyerle, and E. E. Chia, “Phonon mode transformation across the orthorhombic tetragonal phase transition in a lead iodide perovskite $CH_3NH_3PbI_3$: a terahertz time-domain spectroscopy approach,” J. Phys. Chem. Lett. 7(1), 1–6 (2016).
42. M. Grechko, S. A. Bretschneider, L. Vietze, H. Kim, and M. Bonn, “Vibrational Coupling between organic and inorganic sublattices of Hybrid Perovskites,” Angew. Chem. Int. Ed. 57(41), 13657 (2018).
43. F. Brivio, J. M. Frost, J. M. Skelton, A. J. Jackson, O. J. Weber, M. T. Weller, A. R. Goni, A. M. A. Leguy, P. R. F. Barnes, and A. Walsh, “Lattice dynamics and vibrational spectra of the orthorhombic, tetragonal, and cubic phases of methylammonium lead iodide,” Phys. Rev. B. 92(14), 144308 (2015).
44. A. A. Bakulin, O. Selig, H. J. Bakker, Y. L. Rezus, C. Muller, T. Glaser, R. Lovrincic, Z. Sun, Z. Chen, A. Walsh, J. M. Frost, and T. L. Jansen, “Real-time observation of organic cation reorientation in methylammonium lead iodide perovskites,” J. Phys. Chem. Lett. 6(18), 3663–3669 (2015).
45. P. U. Jepsen, “Phase Retrieval in Terahertz Time-Domain Measurements: a “how to” Tutorial,” J. Infrared, Millim. Terahertz Waves 40(4), 395–411 (2019).
46. J. Lloyd-Hughes, N. Chopra, J. Develikis, R. Pandya, and J. Woolley, “A Tutorial on THz Pulse Analysis: Accurate Retrieval of Pulse Arrival Times, Spectral Energy Density and Absolute Spectral Phase,” J. Infrared, Millim. Terahertz Waves 46(6), 34 (2025).
47. R. Koalla, and A. K. Chaudhary, “Cross-correlation technique for phase error correction in reflection mode terahertz time-domain spectroscopy,” Appl. Opt. 63(17), 4762–4772 (2014).
48. J. Neu, and C. A. Schmuttenmaer, “Tutorial: An introduction to terahertz time domain spectroscopy (THz-TDS),” J. Appl. Phys. 124(23), 231101 (2018).
49. P. U. Jepsen, D. G. Cooke, and M. Koch, “Terahertz spectroscopy and imaging: Modern techniques and applications,” Laser Photonics Rev. 5(1), 124–166 (2011).
50. G. Hecht, Optics, 5th ed. (Pearson, Boston, 2017).

Tables

Table 1

Lorentz harmonic oscillator parameters extracted from THz spectra. Resonance frequency (ω_0), oscillator strength (ω_p), damping constant (γ), DC dielectric constant (ϵ_{DC}) and high-frequency dielectric constant (ϵ_∞) obtained from fitting the real part of the complex conductivity and dielectric constant spectra of Sample 1 before and after timing correction (+ 0.02 ps).

	j	$\varvec{\omega}_0$ (THz)	$\varvec{\omega}_{\varvec{p}}$ (THz)	$\varvec{\gamma}$ (THz)	$\varvec{\epsilon}_{\varvec{DC}}$	$\varvec{\epsilon}_\infty$
Sample 1 (+ 0.00 ps)	j =1	0.89	0.37	0.25	-13.4	-13.7
	j =2	1.67	0.65	0.52		
Sample 1 (+ 0.02 ps)	j =1	0.9	0.34	0.22	32.8	32.5
	j =2	1.72	0.69	0.6		

Figures

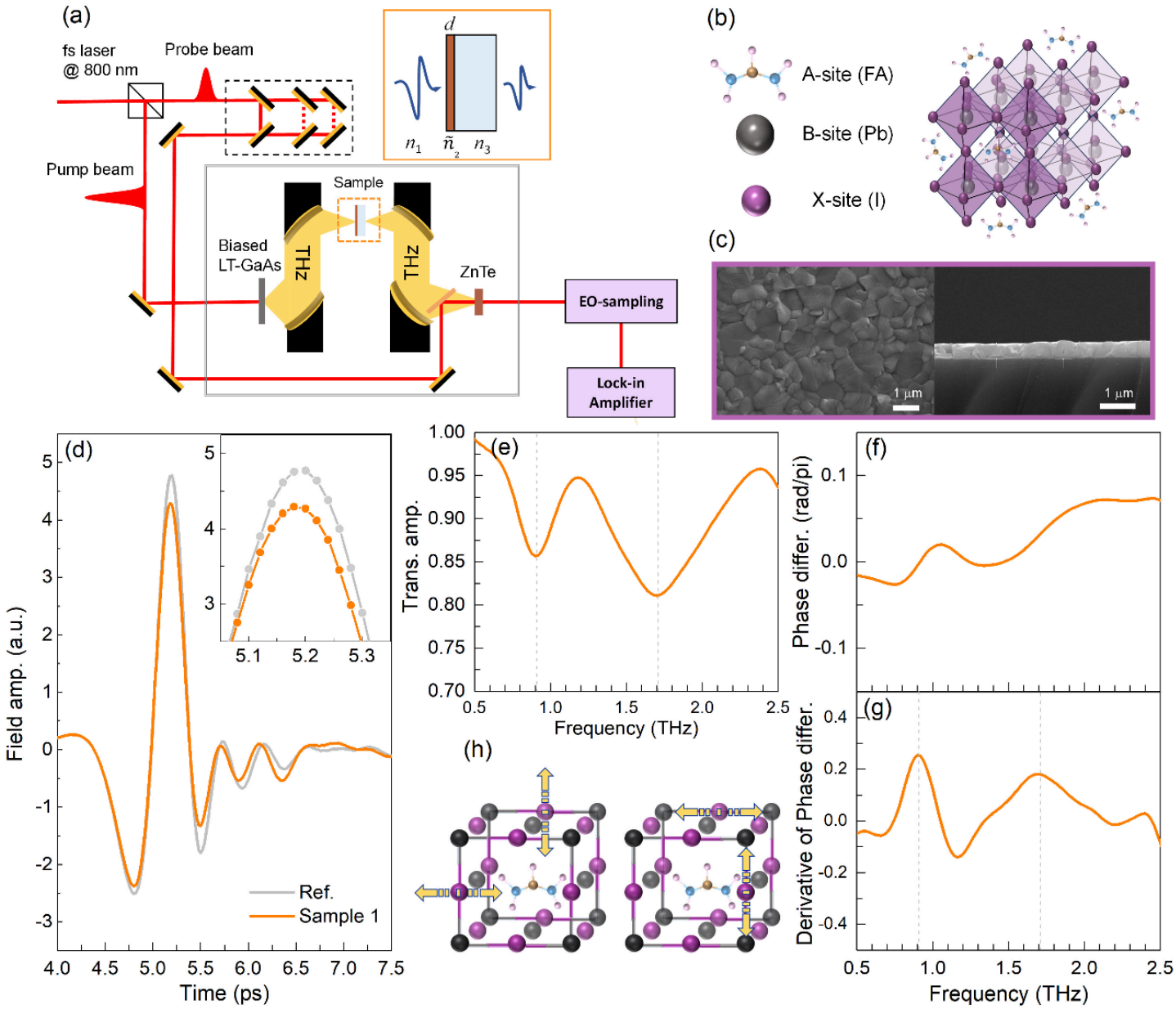


Figure 1

THz spectroscopy of ultrathin $FAPbI_3$ film. (a) Schematic of the transmission-mode THz-TDS setup and measurement geometry, showing air (n_1), the sample (n_2, thickness d), and the substrate (n_3). (b) Crystal structure of the ABX_3 hybrid perovskite, cubic *a*-phase of $FAPbI_3$. (c) SEM images of the ultrathin $FAPbI_3$ film: top-view (left) showing grain size and crystallinity, and cross-sectional view (right) showing film thickness. (d) Time-domain THz waveforms of the reference substrate (gray) and Sample 1 (orange). (e–g) Transmitted amplitude (e), phase difference (f) and derivative of the phase (g) spectra obtained by Fast Fourier transform (FFT). (h) Schematic illustration of the transverse optical (TO) and longitudinal optical (LO) phonon modes near 0.9 THz, 1.7 THz.

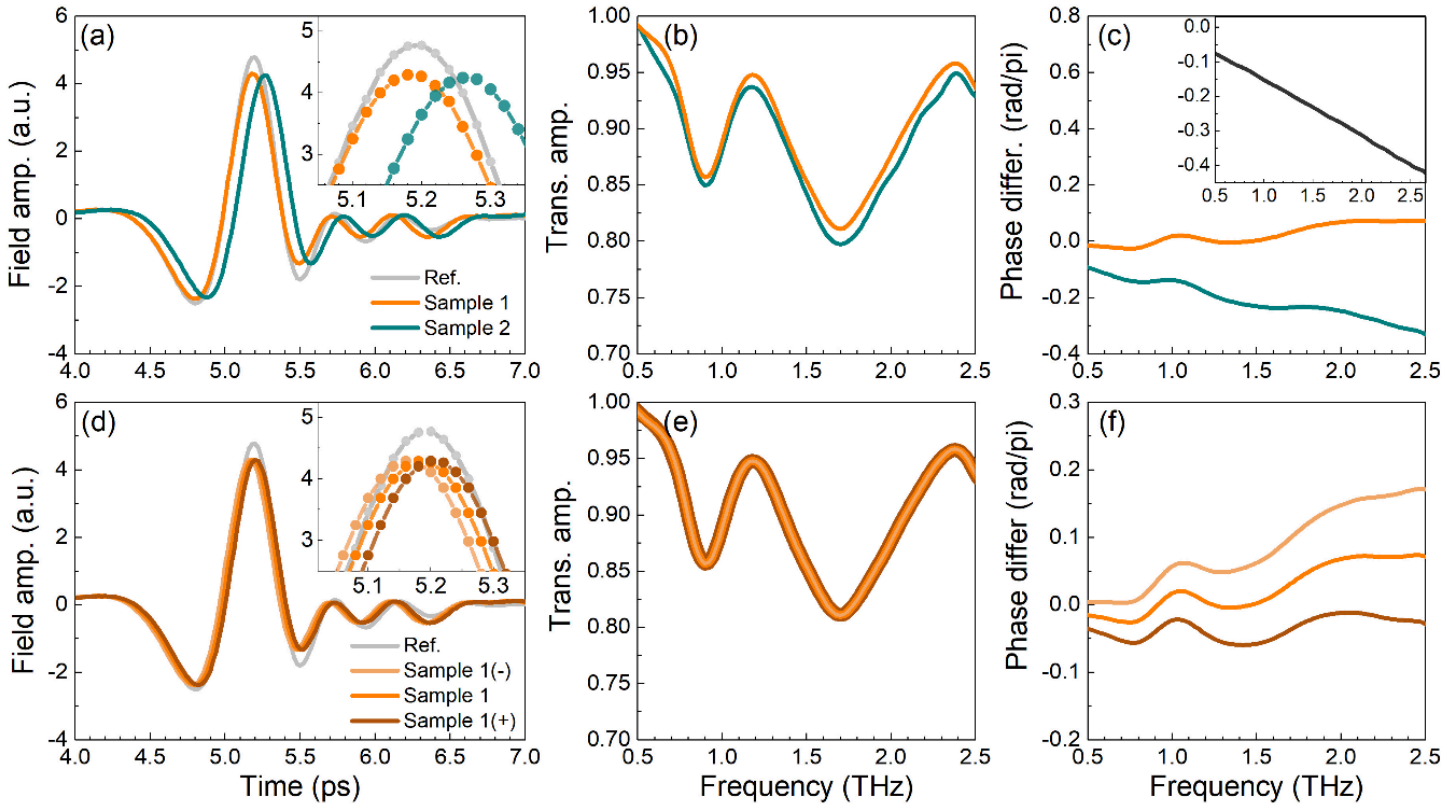


Figure 2

Influence of substrate mismatch and temporal offsets on the THz transmission spectra. (a) Time-domain THz waveforms measured for the reference substrate (gray) and Samples 1 (orange) and 2 (olive). The inset highlights the difference in the peak positions of the waveforms, indicating a small temporal shift between the signals. (b) Transmitted amplitude spectra obtained from the FFT of the time-domain signals. (c) Corresponding phase difference spectra. The inset shows the nearly linear phase shift between Sample 2 and Sample 1 in the 0.5–2.5 THz range. (d) Time-domain waveform of Sample 1 after applying artificial timing corrections with negative (−), nominal, and positive (+) temporal offsets. The inset shows the corresponding peak shifts introduced by the temporal offsets. (e) Transmitted amplitude spectra after applying the timing corrections. (f) Corresponding phase difference spectra showing the effect of temporal shifts on the transmission phase.

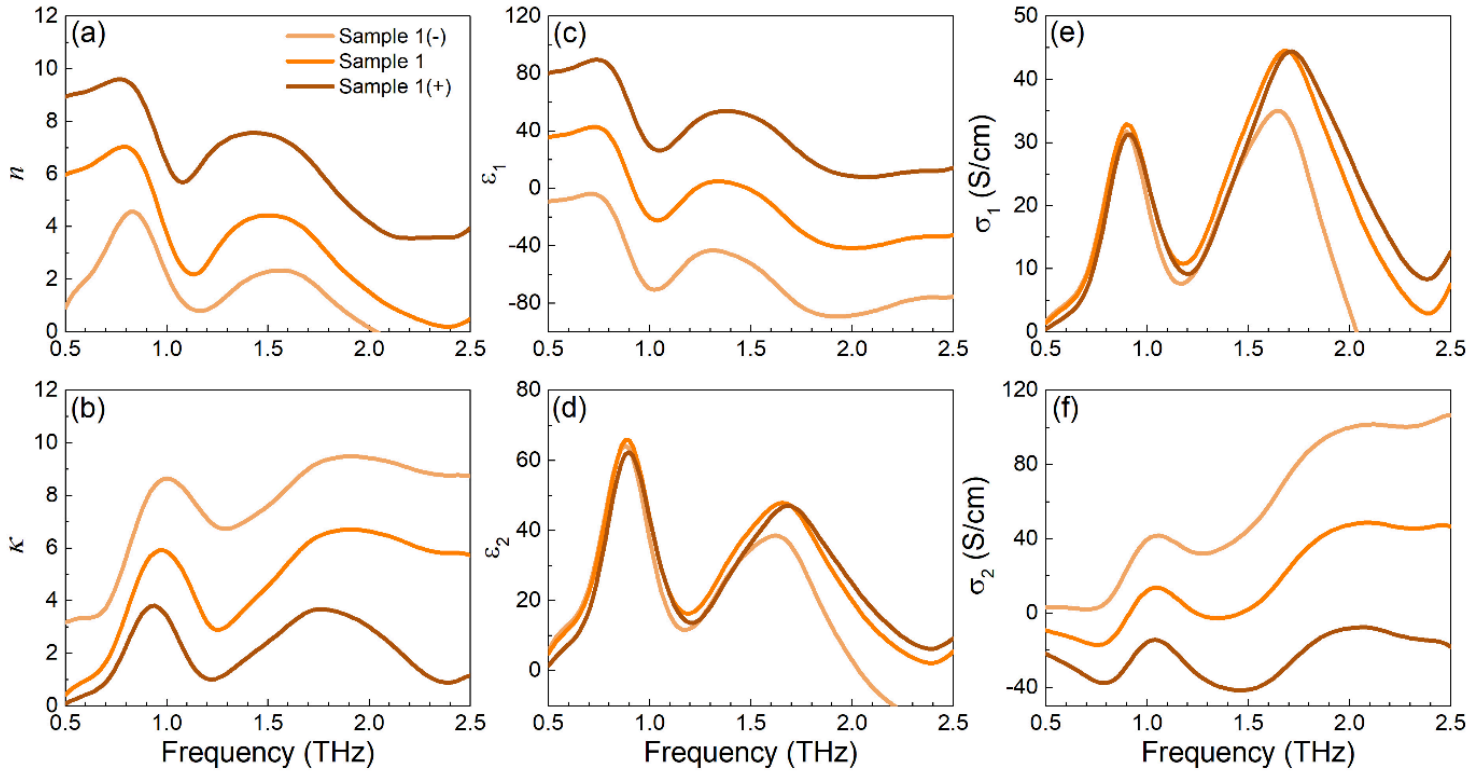


Figure 3

Optical constants extracted from the THz transmission spectra. (a, b) Real and imaginary parts of the refractive index before and after timing-error correction. (c, d) Real and imaginary parts of the dielectric constant. (e, f) Real and imaginary parts of the complex conductivity. All optical properties were obtained using a transfer-function method that accounts for multiple reflections within the ultrathin $FAPbI_3$ film and the thick substrate.

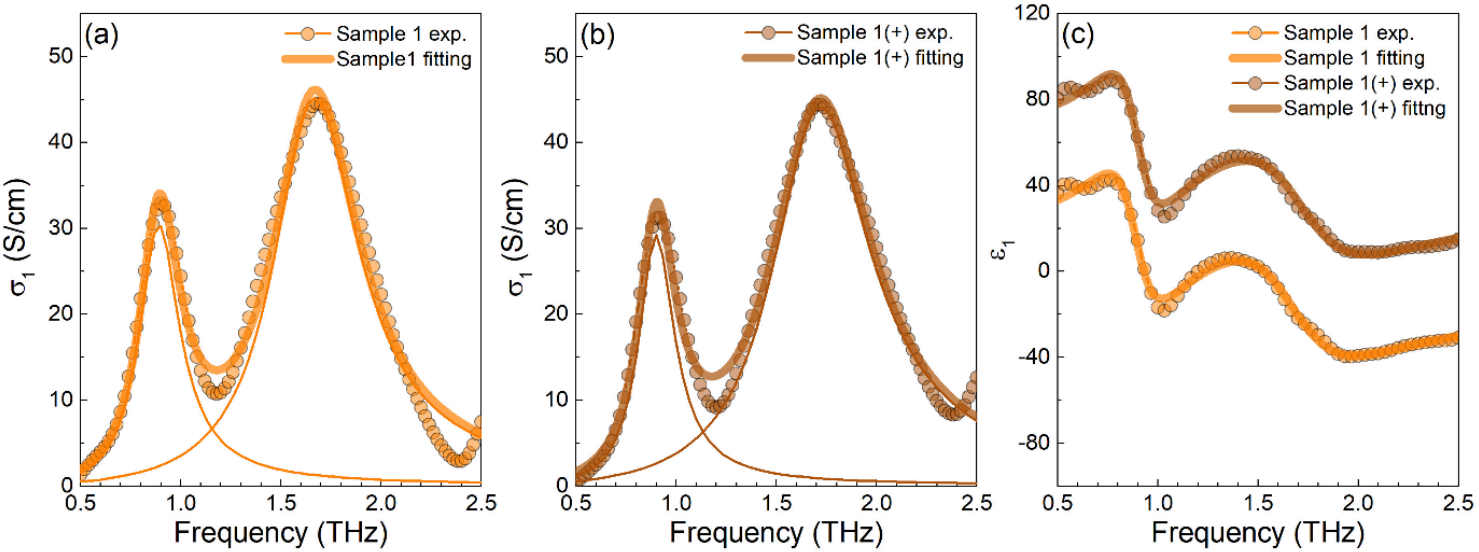


Figure 4

Lorentz oscillator model fitting of the extracted optical properties. (a, b) Extracted real part of the complex conductivity (dotted lines) and the corresponding Lorentz oscillator fits (solid lines) for Sample 1 before (a) and after (b) timing-error correction (+0.02 ps). (c) Extracted real part of the dielectric constant (dotted lines) and the corresponding Lorentz oscillator fits (solid lines) before and after the timing-error correction. The fits reproduce the resonance features accurately while revealing a noticeable shift in the dielectric baseline after timing correction.

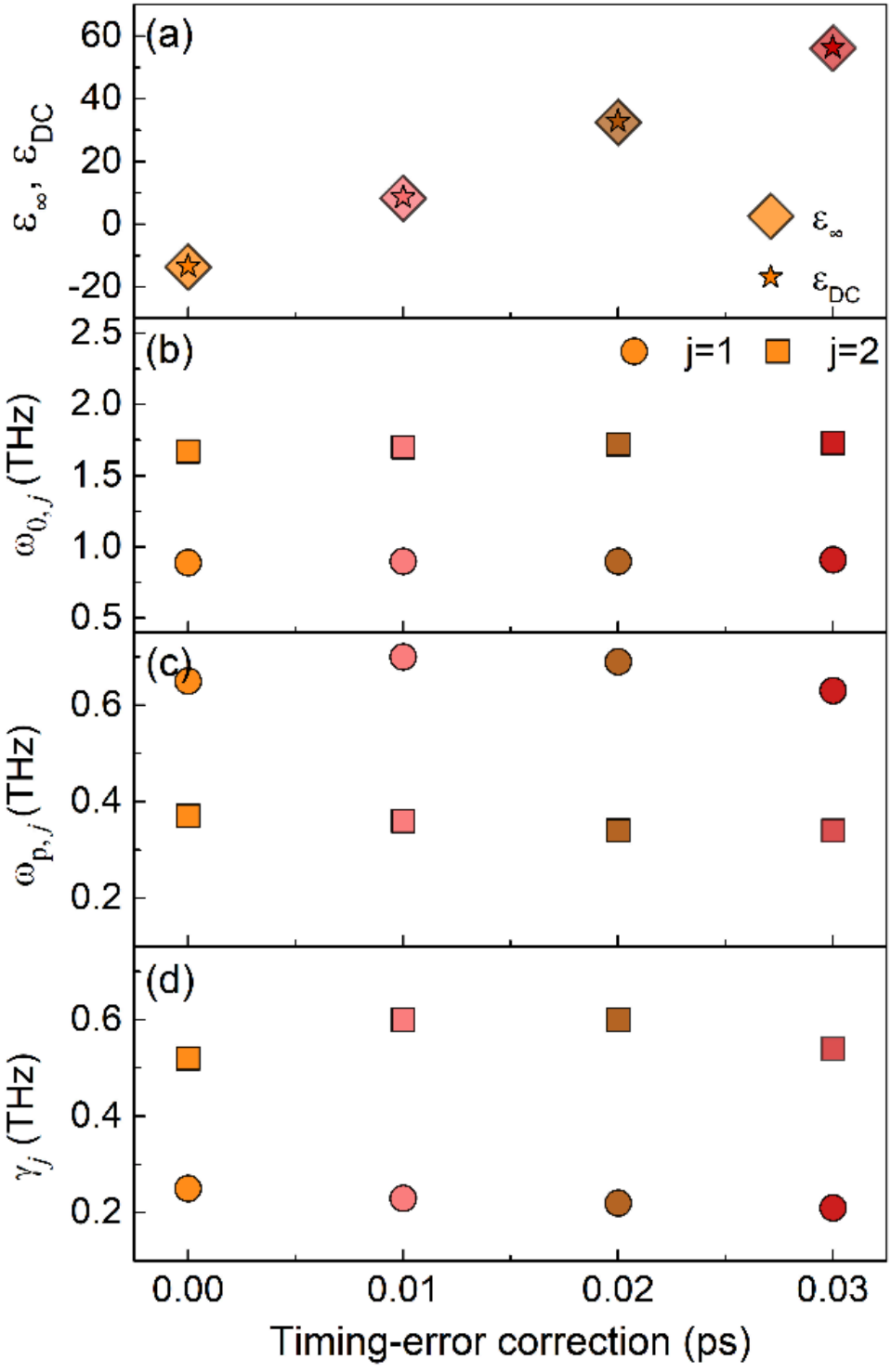


Figure 5

Lorentz oscillator parameters as a function of applied timing correction. (a) DC dielectric constants and high-frequency dielectric constants obtained from the fitted Lorentz harmonic oscillator model for each timing correction (+0.00 ps, +0.01 ps, +0.02 ps, +0.03 ps). (b–d) Resonance frequency (ω_0), oscillator strength (ω_p), and damping constant (γ) extracted from the Lorentz model before and after applying sub-picosecond timing correction. All parameters were obtained by fitting the experimentally extracted real part of the complex conductivity.

Supplementary Files

This is a list of supplementary files associated with this preprint. Click to download.

- 20260331Supplementaryinformationmh.pdf